Mon. Not. R. Astron. Soc. **000**, 000–000 (1999)

X-ray iron line variability for the model of an orbiting flare above a black hole accretion disc

Mateusz Ruszkowski
Institute of Astronomy, Madingley Road, Cambridge CB3 0HA

25 June 1999

ABSTRACT
The broad X-ray iron line, detected in many active galactic nuclei, is likely to be produced by fluorescence from the X-ray illuminated central parts of an accretion disc close to a supermassive black hole. The time-averaged shape of the line can be explained most naturally by a combination of special and general relativistic effects. Such line profiles contain information about the black hole spin and the accretion disc as well as the geometry of the emitting region and may help to test general relativity in the strong gravity regime. In this paper we embark on the computation of the temporal response of the line to the illuminating flux. Previous studies concentrated on the calculation of reverberation signatures from static sources illuminating the disc. In this paper we focus on the more physically justified case of flares located above the accretion disc and corotating with it. We compute the time dependent iron line taking into account all general relativistic effects and show that its shape is of very complex nature, and also present light curves accompanying the iron line variability. We suggest that future X-ray satellites like XMM or Constellation-X may be capable of detecting features present in the computed reverberation maps.

Key words: accretion, accretion discs - black hole physics - galaxies: active - galaxies: Seyfert - X-rays: galaxies

1 INTRODUCTION

The most extreme continuum variability in AGN is usually seen in the X-ray spectral band. The X-ray variability power spectrum reveals that low-amplitude fast flickering is an almost permanent feature, but major changes, such as a flare with a large change in luminosity (like doubling) occur much less frequently. The duration of such flares may by of the order of a few thousand seconds (e.g. see figures in McHardy (1989)). Recent spectroscopic observations suggest that such X-ray flux variations can be accompanied by Fe Kα line variability which occurs on a similar time scale (Iwasawa et al. (1996)). This might indicate that the size of the X-ray continuum emitting region is small in comparison with other sources contributing to the overall continuum and that the iron line is produced in a compact region close to the continuum source and is correlated with the X-ray outburst. The X-ray emission is thought to originate from the innermost part of the accretion disc. This region is subject to a number of instabilities which may produce flare-like activity. There is a large body of observational and theoretical work which supports this view. Among the proposed scenarios invoked to explain such a phenomenon are: the amplification of magnetic fields in the disc by convection and differential rotation leading to the emergence of magnetic fields carrying hot plasma (Galeev, Rosner & Vaiana, 1979), hot magnetic arcs due to the Parker instability (Chagelishvili, Leminadze & Rogava (1989)), magnetic flares due to explosive release of stored magnetic energy in the accretion disc (Vries & Kuijpers (1992)) and vortices (Abramowicz et al. (1992)). The fluorescent iron line emission may be produced by irradiation of the disc material by such flares located above the accretion disc (Lightman & White (1988), George & Fabian (1991), Matt, Perola & Piro, (1991)). As a result, the observed time-averaged spectra have distinctive, skewed, double-peaked profiles which reflect the Doppler and gravitational shifts in a strongly curved spacetime (Fabian et al. 1989, Laor 1991, Mushotzky et al. (1995), Tanaka et al. (1995), Nandra et al. (1997)). Apart from the line emission, the disc material should also reflect a part of the X-ray continuum. Evidence for this effect was found by Pounds et al. (1990) for a number of Seyfert galaxies. Since the spectral properties of the Fe Kα line are well known, the iron line may be used as a probe of the very near environment of a black hole and the black hole itself. This may enable one to study the geometry of the emission region, estimate black hole masses or search for the dragging of inertial frames. The frame dragging effect is especially interesting because

its presence, in cooperation with the shear viscosity of an accreting material, may be responsible for the alignment of an accretion disc symmetry axis with the spin axis of a black hole or help to explain the stability of jets (Bardeen & Peterson (1975)).

Much theoretical work has been done to search for the signatures of the mass and spin parameter of black holes as well as the geometry of the line and continuum emitting regions. Laor (1991) realized the importance of the impact of general relativistic effects in the vicinity of the rotating black hole on the line shape. This influence of the black hole spin on the iron line was later quantified by Dabrowski et al. (1997). They calculated the iron line profile assuming that the line is produced in the thin corona above the accretion disc. They considered the case of the Seyfert 1 galaxy MCG-6-30-15 and concluded that the very broad and skewed iron line can be explained if the emission originates from the disc extending down to the radius of marginal stability $r_{ms} < 1.23$m which corresponds to the spin parameter $a > 0.94$. Thus they claimed that the black hole is rapidly rotating and should be described by Kerr geometry. A similar conclusion was drawn by Bromley, Chen, & Miller (1997) who suggested that the iron line profile was more likely to originate from a disc about a rotating black hole. Another approach was presented by Reynolds & Begelman (1997) (hereafter RB97) who were able to explain the same data by assuming Schwarzschild geometry (i.e non-rotating black hole) and including the matter below the innermost stable orbit. However in their model the iron line was excited by an external flare located on the symmetry axis above the accretion disc and illuminating the regions below the innermost stable orbit. They also claimed that the rapidly rotating black hole in the radio-quiet active galaxy MCG-6-30-15 is contrary to some theoretical models invoked to explain radio loudness in AGN (e.g. Rees et al. (1982), Wilson & Colbert (1995)). However more recent studies show that this is not necessarily the case (Ghosh & Abramowicz (1997), Livio, Ogilvie & Pringle (1999)). Recently Young, Ross & Fabian (1998) calculated the spectrum corresponding to the RB97 model and found that it should possess a photoelectric absorption edge of iron, which is not seen in the data. However with the quality of the current data the issue of the black hole spin remains ambiguous. An entirely different approach to searching for the observational signatures of the black hole spin, mass and the geometry of emission region was first suggested by Fabian et al. (1989) and later considered in any detail by Stella (1990). He computed the iron line variability from a disc around a Schwarzschild black hole assuming a pointlike variable X-ray source located in the geometric centre of the disc. For an observer at infinity any such variations of the primary X-ray source would be 'echoed' by different locations on the disc leading to time evolution of the line profile. The primary goal of this research was to suggest a method to estimate black hole masses. His work was extended by Matt & Perola (1992) and Campana & Stella (1993, 1995) who considered modified source geometries. Recently Reynolds et al. (1999) (hereafter RYBF99) generalized these results by assuming arbitrary black hole spin and searched for observational signatures of this parameter. They mainly focused on the case of on-axis source but briefly discussed preliminary results for a static flash-like off-axis flare in the vicinity of a Kerr black hole.

As noted above, the duration of bright flares can be of the order of $100m_7$ in geometric time units ($1Gm_710^7\,\mathrm{M}_\odot/c^3 \approx m_749s$; for the black hole mass $M = 10^7 m_7\,\mathrm{M}_\odot$). It is very likely that any variability associated with blobs above accretion discs most likely comes from moving sources. Thus in general, the assumptions of a static primary X-ray source made in previous studies, and in particular the assumption of an δ-like flash from a static flare made by RYBF99, limit the applicability of their results. In the present work we relax these assumptions and consider reverberation effects from corotating flares above an accretion disc. We take into account the effect of Doppler boosting of radiation from a moving flare which was neglected by RYBF99 and allow the flares to revolve around a black hole. We calculate the time dependent iron line for different values of inclination of the accretion disc and spin parameter (we consider the Schwarzschild and the almost maximal Kerr cases) and different positions of the flare relative to the accretion disc. We also compute the light curves accompanying the iron line variations including the direct flux from the flare and the reflected flux from the disc. Similar calculations were performed for example by Bao (1992), Karas et al. (1992), Zakharov (1994) and Bromley et al. (1997) in the context of corotating spots located on the accretion disc.

The following Section and its subsections describe the assumptions made in our model and the algorithm used to simulate the light curves and the iron line flux variations. The last Section is devoted to the presentation and discussion of our results.

2 THE MODEL ASSUMPTIONS AND THE ALGORITHM

2.1 The X-ray flare and the disc illumination

We assume that the primary source of radiation is an X-ray flare situated above the accretion disc. As noted in the introduction, magnetic instabilities may cause such a flare to emerge from the disc and its position relative to the disc surface may remain approximately unchanged for some time. Thus we make the assumption that the flare is confined by the magnetic field and corotates with the disc and possesses fixed Boyer-Lindquist coordinates r and θ. We also assume that: the flaring region is point-like, has a finite life-time and that photons propagate freely to either the observer, to the black hole, to the disc or escape to infinity once emitted by the blob. This means that the corona above the accretion disc is optically thin. This is a generalization of the considerations presented by RYBF99 who model X-ray flare as a $\delta-$like impulse and additionally assume that radiation is produced in the locally non-rotating frame of reference. In order to numerically integrate the photon trajectory from the *corotating* flare we first analytically derive appropriate constants of motion to propagate photons through the Kerr metric. All the necessary formulae are given in Appendix B, where we express the constants of motion in terms of polar and azimuthal angles in the local rest frame of the point-like source. Thus we can easily model the isotropic distribution of radiation in the emitter's frame by a Monte Carlo method. This enables us to calculate the illuminating flux as a function of time and energy in the rest frame of the

corotating disc material taking into account all the general relativistic effects, including previously neglected Doppler boosting from the moving flare. In the implementation of the algorithm we used the formula (see Appendix C):

$$F(E_d, \tilde{t}_{sd}) \propto S_{E_d} = g_{sd}^{1+\alpha} E_d^{-\alpha} \frac{f_{sd}}{\gamma d\phi dr} \left(\frac{\Delta}{A}\right)^{1/2},$$

where we additionally assume that the flare emits a power law spectrum with energy index α. The factor f_{sd}, which is the ratio of the number of photons intersecting a small patch on the disc (defined by $d\phi$ and dr) to the total number of emitted photons, was calculated by means of the Monte Carlo method. In the above formula $\tilde{t}_{sd}$ is the time it takes for photon emitted from the source to reach the disc element and γ is the Lorentz factor for the relative motion of the disc element and the locally non-rotating observer. g_{sd} is the redshift factor given by

$$g_{sd} = \frac{u_d^\mu p_{d\mu}}{u_s^\mu p_{s\mu}},$$

where $p_{d\mu}$ and $p_{s\mu}$ are the photon four-momenta at the disc and source respectively. We follow the lines of reasoning of Cunningham (1975) and split the velocity field of the accretion disc u_d into the region outside the radius of marginal stability, where matter follows circular orbits, and the region within the innermost stable orbit where the matter has a negative radial component and spirals towards the black hole. The formulae for the flare velocity field u_s^μ are collected in Appendix B.

2.2 Reprocessing of radiation by the accretion disc

The radiation which impinges upon the disc surface is reprocessed and reflected. The shape of the reflected spectrum depends upon many factors, the most important being the disc structure and ionization state of the accretion disc. In the subsequent discussion we assume the disc to be optically thick and geometrically thin. The optical depth of the accretion disc was calculated by many authors (e.g. Frank, King, & Raine. (1995), RB97) and is shown to be large. This guarantees that the illuminating radiation can be efficiently reflected. However the albedo of the reflecting material depends on the ionization parameter which varies across the disc surface: $\xi(r,\phi) = 4\pi F_X(r,\phi)/[n(r)\cos n]$, where $n(r)$ is the comoving electron number density given by Eq. 4 of RYBF99, $\cos n$ is the angle between the incident rays and the normal to the disc surface in the comoving frame of the disc and F_X is the X-ray flux defined over some fixed energy band at a particular position on the disc. We calculate the parameter ξ and use the results of Ross, Fabian & Young (1998) to calculate the albedo $a_R(E)$ as a function of energy for all grid elements on the disc. We then adopt the simple prescription of RYBF99 to separately model the iron line fluorescence in the rest frame of the moving disc element, i.e. we assume that for $\xi < 100$ erg cm s^{-1} the matter emits cold iron line at 6.4 keV with some yield Y, for ξ in the range from 100 erg cm s^{-1} to 500 erg cm s^{-1} there is no emission because the radiation is destroyed by Auger mechanism, for ξ between 500 erg cm s^{-1} and 5000 erg cm s^{-1} we use a composition of two lines at 6.67 keV and 6.97 keV each with the fluorescent yield Y and assume that no iron line is produced for $\xi > 5000$ erg cm s^{-1} because of total ionization of the matter (here we approximate the iron lines as delta functions). Note that these additional complications are essentially relevant only for the Schwardschild black hole because only in this case can a significant fraction of the disc material within the innermost stable orbit ($r_{ms} = 6m$) be in the higher ionization state (large ξ). This arises from the fact that the radial density gradient of the matter spiralling towards the black hole is strongly negative in this region so the disc significantly decreases its density whereas the density changes for radii greater than r_{ms} are comparatively negligible and the disc remains relatively dense and thin, at least for small accretion rates. This means that the disc may be treated as approximately cold for $r > r_{ms}$ and the variations of the ionization parameter induced by the density changes should not dramatically alter the reflection from the disc in this region. Thus the assumption of RYBF99 about the high density and negligible ionization of the region outside r_{ms} in the Schwarzschild case may be justified. In the Kerr case the radius of marginal stability asymptotically approaches the event horizon and we assume that the disc may be approximated as being cold on average. The results of Różańska et al. (1998), who show that the presence of a hot corona makes the disc denser and less ionized, further strengthen the above argument.

In the subsequent considerations we use the additional simplifying assumption of isotropic reflection and write the reflected intensity in the form:

$$I_R(E_d, \tilde{t}_{sd}) = \frac{1}{\pi} a_R(\xi, E_d) F(E_d)$$

2.3 Calculation of light curves and iron line variability

In order to calculate the time-varying iron line profiles and the corresponding continuum light curves we used the following prescription:

1) We use a ray-tracing technique to follow the trajectories of photons from positions (x, y) on the observer's image plane to the disc, keeping track of all Boyer-Lindquist coordinates $\tilde{t}_{do}(x,y)$, $r(x,y)$, $\theta(x,y)$, $\phi(x,y)$, until the photons either intersect the accretion disc plane or disappear below the event horizon (The observer is located at $r = 1000m$, $\theta = i$ and $\phi = 0^o$, where i is the inclination). We then calculate the redshift factor corresponding to the particular final position of a photon and its arrival time from the disc. We generate an image of approximately 1600×1600 pixels covering roughly an area of $160m \times 160m$.

2) Using the time dependent ionization and illumination pattern described above and albedo $a_R(E, \xi)$, we specify the emergent flux from the disc as a function of time and energy in the fixed spectral band, i.e. we integrate all photons coming from regions of equal arrival time regions on the accretion disc at a particular energy. In doing so we also take into account the fact that the source changes its position and rotate the illumination and ionization patterns accordingly. This allowed us to compute the reflected spectrum as a function of time and thus the reflected component of the light curve. We use the following formulae (see appendix C for additional explanations):

$$F_R(t) = \sum_n F_R^{(n)}(t),$$

where $F_R^{(n)}(t)$ is the contribution to the flux from the flare at the n-th position given by:

$$F_R^{(n)}(\tilde{t}) = \frac{1}{\Delta\tilde{t}} \sum_{\tilde{t}\rightarrow\tilde{t}+\Delta\tilde{t}} C(E_{o1}, E_{o2}, \alpha) \int\int_{E_{o1}}^{E_{o2}} g_{do}^3 I_R(E_o/g_{do}) dE_o \frac{dxdy}{r_o^2},$$

where g_{do} is the redshift factor for the disc-to-observer case, $dxdy$ is the pixel surface area on the observer's image plane, r_0 is the distance from the black hole system and $\tilde{t} = \tilde{t}_{sd} + \tilde{t}_{do}$.

3) We compute the direct flux component by propagating photons from the source to the observer. We use a formula analogous to that above to calculate this flux.

4) Having specified the illumination pattern and ionization state for a given position of the flare above the accretion disc, we determine the contribution of each grid element on the disc surface to the iron line profile from the formula:

$$\Psi^{(n)}(E, \tilde{t}) \propto \frac{1}{\Delta\tilde{t}\Delta E} \sum_{\tilde{t}\rightarrow\tilde{t}+\Delta\tilde{t}, E\rightarrow E+\Delta E} Y(\xi, E/g_{do}) g_{do}^4 F_X(r, \phi),$$

where $F_X(r, \phi)$ is the integrated over a fixed energy band X-ray flux at the given position on the disc. The above function is the Green's function (transfer function) corresponding to the n-th position of the flare.

5) In the last step we use the transfer functions for single isolated flares in order to calculate the observed iron line flux variations. We use the following expression:

$$F_{Fe}(E, t) \propto \sum_n \Psi^{(n)}(E, t),$$

where we also take into account the delays due to the revolution of the flare around the black hole. As in the case of the reflected flux, we interpolate the contributions to the flux from the isolated flares and then add the interpolated fluxes. Note that the binning of the transfer functions in time would introduce a small additional (artificial) flux variability, because we physically rotate the illumination pattern. This is because the differences between the arrival times from the neighbouring disc elements on the approaching side of the disc would be shorter compared to the corresponding differences on the opposite side.

3 RESULTS

We present iron line flux variations and the corresponding light curves for one full revolution of the flare around the black hole with a step-like luminosity variation in the local frame of reference of the flare. This is for illustrative purposes and we stress that while it is trivial, for example, to generalize the code to include arbitrary intrinsic luminosity variations in the rest frame of the flare, we do not wish to complicate the interpretation of the results. Future observations may guide us as to how to introduce additional modifications in the computations. The results in the present form can in principle be applied to the case of isolated flares or at least strong outbursts accompanied by minor ones. In the computations we assume that the source emits a power law spectrum with energy index $\alpha = 1$.

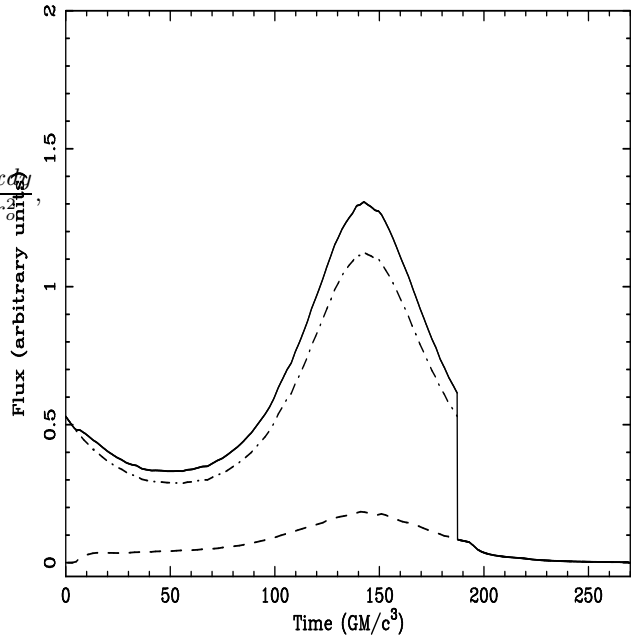

Figure 1. Total light curve (solid line), the direct flux from the flare (dot-dashed line) and the small contribution from the reflected component (dashed line) for the same set of parameters as in Fig. 3. The flare is switched on from $\phi = 0^o$ to $\phi = 360^o$.

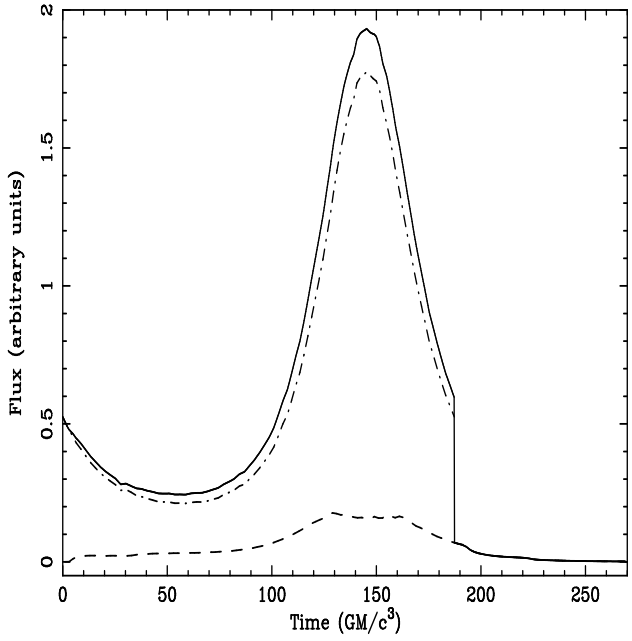

Figure 2. Total light curve (solid line), the direct flux from the flare (dot-dashed line) and the small contribution from the reflected component (dashed line) for the same set of parameters as in Fig. 4. The flare is switched on from $\phi = 0^o$ to $\phi = 360^o$.

Fig.1 and Fig.2 present the light curves. The light curves are a superposition of the direct flux from the flare and the reflected flux from the disc. The small offset between these two components (note the shift between initial and final times of the reflected and direct flux) is due to the additional time photons need to propagate towards the disc and back. The small albedo of the disc material in the chosen energy band (2-9 keV) results in a relatively small contribution from reflection continuum to the total light curve. However the albedo strongly increases with energy and thus the reflection would be much more efficient in the harder part of the observed spectrum. Another effect which would enhance the reflected component (and suppress the direct one) is the focusing of light from the flare. More radiation from the flares closer to the central black hole would be focused towards the disc and reflected, and simultaneously less direct flux would reach the observer (Martocchia & Matt, (1996)). The peaks in the direct light curve are mainly attributed to the Doppler effect. Note how the flux variability is enhanced by the inclination of the system. For higher inclinations the Doppler effects are more pronounced and the peaks are narrower and have higher maxima. It is important to note that the flux variability observed in the chosen spectral band (2-9 keV in our case) is also a function of the energy index and will be increased in the case of the steeper spectra. The peaks due to gravitational focusing (e.g. Cunningham & Bardeen, (1973)) are not seen here because we limit our discussion to low inclinations in order to avoid additional complications related to the limb darkening. This is not a serious limitation to our model because the majority of Seyfert 1 galaxies are likely to have small inclination angles. However we compare our results for the direct flux in the test case of a source orbiting the black hole in the equatorial plane for very high inclinations of the orbit and find agreement with the results of Cunningham & Bardeen (1973).

Figs from 3 to 8 show the evolution of the iron line spectra after the subtraction of the varying power law continuum for different sets of parameters. As for the case of the light curves, the time offset of the initial spectrum is the difference between the arrival of the direct continuum flux and the first appearance of the iron line. There is a clear difference between the results for the two considered extremal values of the spin parameter (e.g. compare Fig. 4 and Fig.6). The iron line extends to lower frequencies in the Kerr case which is due to the cold iron line being produced very close to the black hole. The influence of the ionization of the accretion disc below the radius of marginal stability $r_{ms} = 1.23m$ is relatively unimportant. On the contrary, in the case of the Schwarzschild black hole the bulk of the cold iron line is produced only above $r_{ms} = 6m$ and accretion disc may be in highly ionized within this radius. Thus for $r < 6m$ the line may be either destroyed by the Auger process or not produced because of the total ionization of the disc material. The radiation from this region would be subject to high energy shifts which means that the lack of the iron line flux at lower energies (see Fig. 5 and Fig.6) is the result of the fact that some parts of the disc below $r_{ms} = 6m$ cannot produce the iron line. For the flare at the position ϕ_{flare} the regions on the disc responsible for the production of the iron line in the higher ionization states (500 erg cm s^{-1} $< \xi <$ 5000 erg cm s^{-1}) are located around $\phi = \phi_{flare} \pm 90^o$. The regions on the opposite side of the black hole ($\phi = \phi_{flare} + 180^o$) and

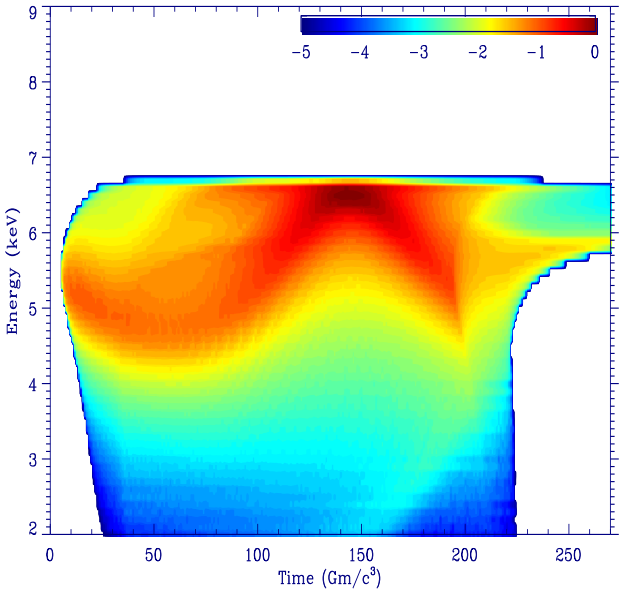

Figure 3. The colour map represents time-sequence of the iron line spectrum, i.e. log(F(time,energy)), where F is the flux divided by the maximum flux during the whole time interval. The Boyer-Lindquist coordinates of the flare are: $\theta_{flare} = 70^o$, $r_{flare} = 10m$ with ϕ_{flare} changing from 0^o to 360^o. The spin parameter and the inclination are $a = 0.998$ and $i = 30^o$ respectively.

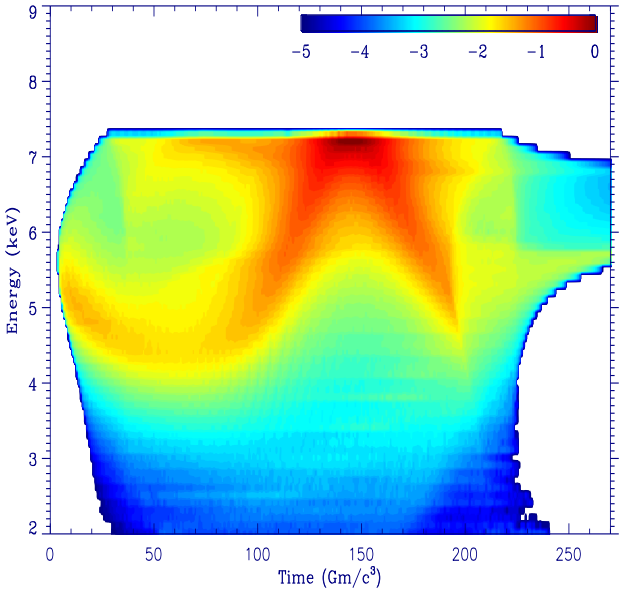

Figure 4. As Fig. 3, but for $i = 50^o$.

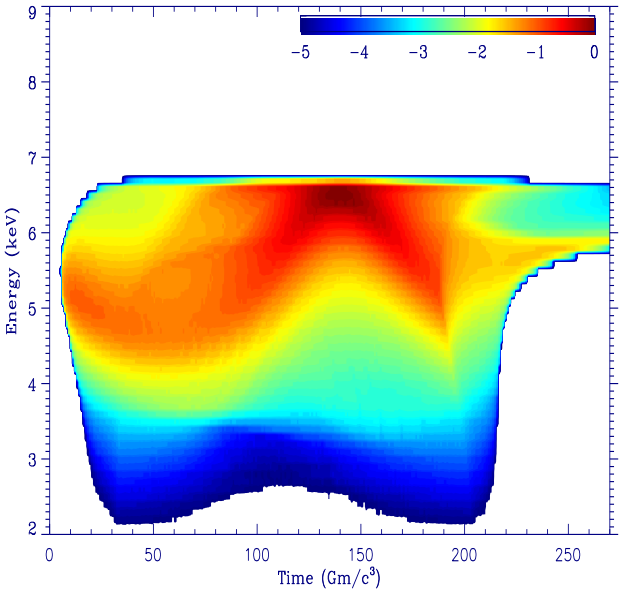

Figure 5. As Fig. 3, but for $a = 0.0$.

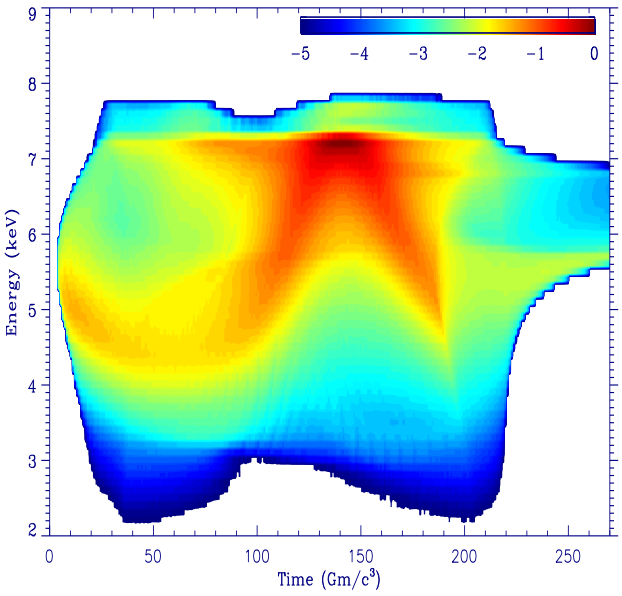

Figure 6. As Fig. 3, but for $a = 0.0$ and $i = 50^o$.

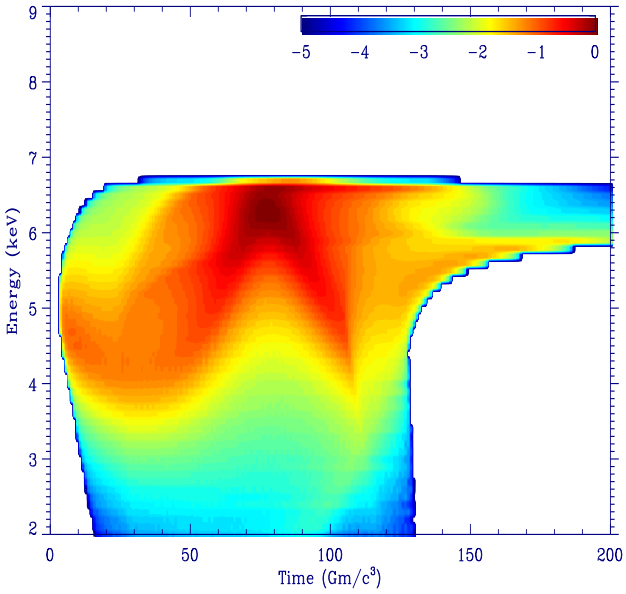

Figure 7. As Fig. 3, but for $r_{flare} = 6.5m$.

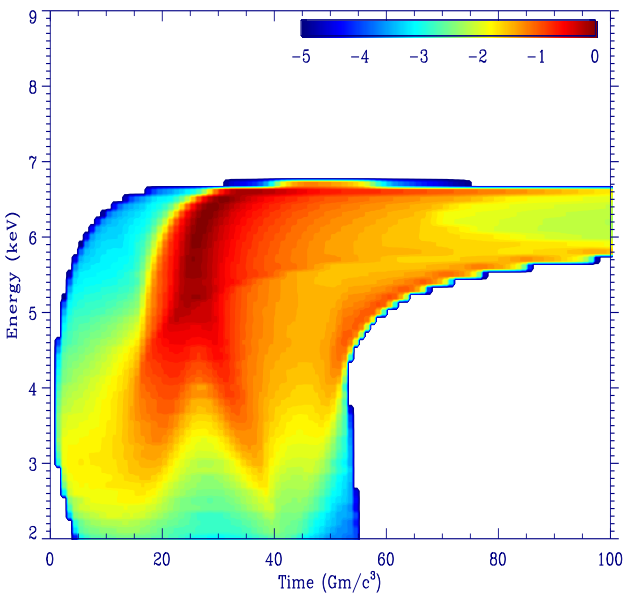

Figure 8. As Fig. 3, but for $r_{flare} = 3m$.

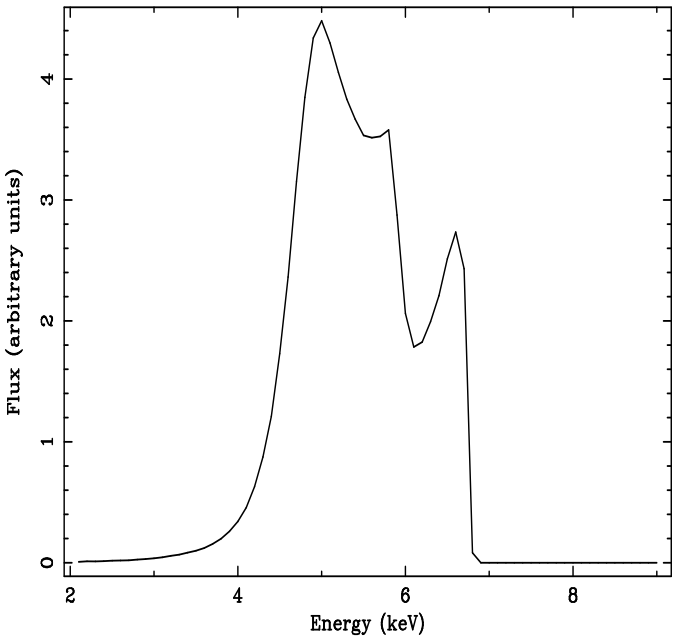

Figure 9. Integrated iron line profile for $t = (70 \div 80)Gm/c^3$ after the detection of the first signal from the flare for: $a = 0.998$, $\theta_{flare} = 70^o$, $r_{flare} = 10m$ and $i = 30^o$

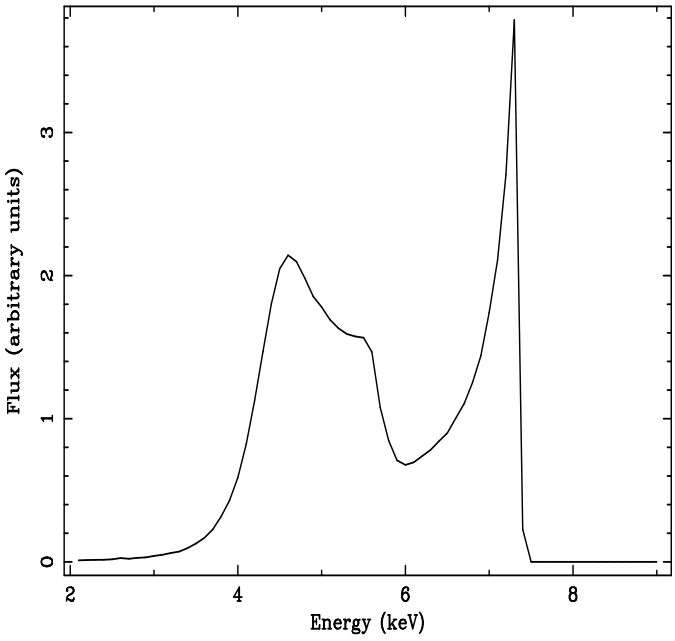

Figure 10. Integrated iron line profile for $t = (70 \div 80)Gm/c^3$ after the detection of the first signal from the flare for: $a = 0.998$, $\theta_{flare} = 70^o$, $r_{flare} = 10m$ and $i = 50^o$

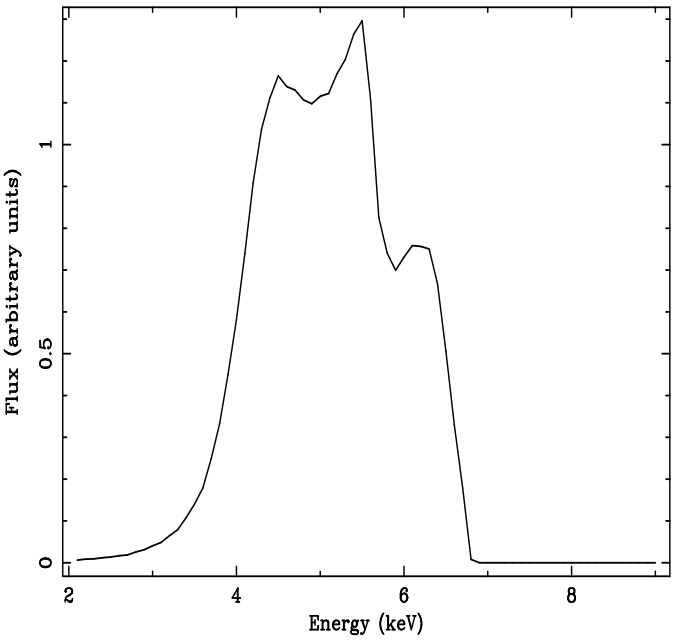

Figure 11. Integrated iron line profile at $t = (40 \div 45)Gm/c^3$ after the detection of the first signal from the flare for: $a = 0.998$, $\theta_{flare} = 70^o$, $r_{flare} = 6.5m$ and $i = 30^o$

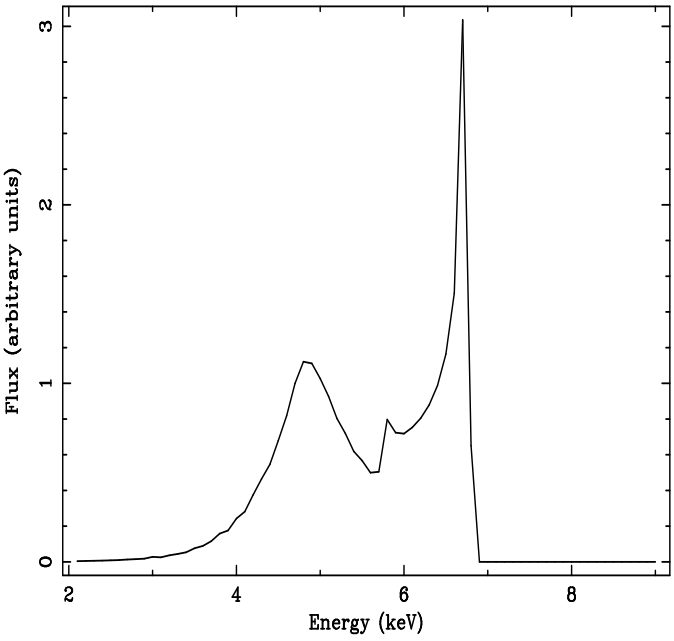

Figure 12. Integrated iron line profile at $t = (50 \div 55)Gm/c^3$ after the detection of the first signal from the flare for: $a = 0.998$, $\theta_{flare} = 70^o$, $r_{flare} = 3m$ and $i = 30^o$

nearest to the flare ($\phi = \phi_{flare}$) have even higher ionization parameter which is the result of the strong light bending and the direct illumination of the disc surface respectively. This effect gives rise to the varying width of the line for $a = 0$ with a minimum around $(100 \div 150)Gm/c^3$ (see Fig.5 and Fig. 6). Future high-throughput instruments like XMM and Constellation-X may be capable of detecting such feature in the temporal iron line profiles. However we stress that a detection of this weak feature would be difficult because it could be overwhelmed by the continuum variations. Other interesting features are the two 'bumps' seen for the inclination $i = 50^o$ and the Schwarzschild black hole. Here the iron line extends to higher frequencies than the maximum frequency in the Kerr case for the same inclination of the disc (compare Fig. 4 and Fig.6). These features are due to the highly blueshifted 'hot' iron lines ($E^{(1)}_{rest} = 6.67$ keV and $E^{(2)}_{rest} = 6.97$ keV) from the ionized regions. This effect should also be within the reach of capabilities of XMM and particularly Constellation-X. It has to be stressed however that the above results are sensitive to the parameters and depend on the position of the flare and its X-ray efficiency (here assumed to be $\eta_X = 0.06$) and the density of the disc below the innermost stable orbit (which is regulated by the half thickness of the disc h_{disc}; here we assumed $h_{disc} = 0.05r$). In principle, a source of very low efficiency located at a very large distance and large θ_{flare} and illuminating the high density region below the innermost stable orbit could not ionize it, and a faint cold iron line could also be produced all the way down to the event horizon in the Schwarzschild case. In such situation it would be difficult to distinguish between the Kerr and Schwarzschild black holes. On the other hand, the flares located closer to the black hole and closer and less inclined with respect to the rotation axis would ionize the regions below the innermost orbit much more efficiently leading to even more pronounced differences (e.g. then those shown in Fig.4 and Fig.6) between the temporal iron line profiles for the two extreme values of the spin parameter. The work of RB97 and Young et al. (1998) has shown that in the special case of a nonrotating black hole and the flare located on the rotation axis very close to the black hole (e.g. $h = 3.5m$) essentially all radiation is focused towards the disc (and the black hole) leading to strong ionization. Young et al. (1998) also demonstrated that in this case the iron absorption edge becomes important. This effect leads to the trough in the iron line spectrum above the considered iron line rest energies. Thus more accurate modelling should include the absorption edge which would decrease the iron line flux from the ionized regions below r_{ms} and create an oscillating absorption feature in the reverberation maps. It is also possible that other processes could influence the iron line production below r_{ms}. For example, the radiation drag could decrease the momentum of the infalling matter and thus accelerate the accretion below r_{ms} leading to a decrease in density and an increase in the ionization parameter in this region. Thus, as a result of the above processes, the iron line in the Schwarzschild case may not extend to frequencies as low as those in the Kerr case and may possess the absorption features, so in general the appearance of the reverberation maps for the two cases should indeed be different, making it possible to distinguish between a rotating and nonrotating black hole.

The most prominent feature seen in all diagrams showing the evolution of the iron line spectrum is the drifting maximum of the flux. This sinusoid-shaped feature is due to the fluorescence from the most strongly illuminated part of the disc located just below the flare. Its shape and brightness is the result of special and general relativistic effects. Initially the flare moves in a direction perpendicular to the line of sight and the maximum is redshifted due to the transverse Doppler effect and gravitational frequency shift. Later it gradually begins to recede from the observer. The brightness of this maximum is suppressed at this stage because the flux from the highly illuminated part of the disc below the flare decreases as a result of light beaming in the opposite direction relative to the observer. The other interesting feature seen in this phase is the double maximum clearly seen around $(50 \div 100)Gm/c^3$ in Fig.4 and Fig.6. As mentioned above, the lower maximum is the result of the redshifting of the bulk of the radiation from below the receding flare. The emerging upper maximum on the other hand, is due to fluorescence from the illuminated regions on the approaching side of the disc. As the flare rotates and enters the approaching side of the disc the bulk of the iron line flux shifts towards high energies and the Doppler boosting of the radiation reflected by the strongly illuminated regions of the disc leads to the rise of the iron line maximum and its brightening. After the flare passes through $\phi_{flare} \approx 270^0$ the energy shift decreases and gravitational and transverse Doppler shifts gradually take over. Note that during the whole revolution of the flare the redshift factor $g < 1$ for a longer time, because the gravitational and transverse Doppler shifts may for some time overwhelm the blueshifts when the flare is on the approaching side of the disc, i.e. when the flare has just entered or is just about to leave the approaching side of the disc. This effect gives rise to a flattening of the minimum (in energy) of the main flux maximum, i.e. the bright Λ-shaped feature appears to be sharper (e.g. see Fig. 4 and Fig. 6).

A very interesting feature can be seen when the flare is receding ($\phi \approx 90^o$). The main redshifted flux maximum broadens (see Fig. 4 and Fig. 6) or even splits into two maxima (see Fig. 3, Fig. 5 or Fig. 7). In order to illustrate this effect better, appropriate cross-sections through the reverberation maps shown in Fig. 3 and Fig. 4 are given (see Fig. 9 and Fig. 10 respectively). Note that in the case of Fig. 9 three maxima are seen. This thickening or splitting is a purely general relativistic effect. The middle maximum is a consequence of strong bending of light which is focused on the opposite side of the black hole relative to the actual position of the flare and leads to the enhancement of the illumination of the disc in this region. The influence of this effect is even more important for the flare located closer to the black hole ($r_{flare} = 6.5m$) as shown in Fig. 7 and Fig. 11. Fig. 11 shows three distinct maxima with the middle maximum due to light focusing being dominant. As in the previous cases, such an effect could be observable by future high throughput spectrometers. The magnitude of the energy shift of the main maximum is related to the inclination of the accretion disc (e.g. compare Fig. 3 and Fig. 4) and also to the distance of the flare from the centre. The latter effect is demonstrated for example in Fig.3, Fig. 7 and Fig. 8 where the bright Λ-shaped feature extends gradually to lower energies as the distance r_{flare} of the flare from the centre decreases. The same figures also illustrate how the timescale of

the sinusoidal variation changes as a function of r_{flare} with shorter time scales corresponding to faster orbital motion of the closer flares. Note how the structures on the reverberation map change for a very close flare ($r_{flare} = 3m$; see Fig. 8). There is no triple maximum on the left hand side of the Λ-shaped feature, but the maximum due to focusing emerges on the opposite side. This is also shown on Fig. 12 where three maxima are visible but, unlike in the case of more distant flares, in this case the lowermost and middle maxima are due to gravitational focusing. The lack of the uppermost and middle maxima on the left hand side of this feature is related to the very large overall gravitational and transverse Doppler redshift. It is also caused by the faster motion of the flare (and thus the main flux maximum) combined with the relatively slow propagation of signals slowed by the Shapiro delay in the vicinity of the black hole. In other words, the ratio between the time it takes for the flare to complete a half of one full revolution around the black hole to the signal crossing time decreases with decreasing distance of the flare from the centre. The above effects contribute to the swamping of these two maxima by the main bright maximum.

We have demonstrated that the very complex behaviour of the lines is predicted by a relatively simple model of the orbiting flare. Our results can be applied to future observations made with XMM and particularly Constellation-X and may help to understand various processes operating in the vicinity of black holes. These results can be used to put constraints on their masses and spin parameters, the geometry of the emitting region and test general relativity in the strong gravity regime. Particularly interesting features seen on our diagrams are the triple maxima in the temporary iron line profiles. The middle maximum is a consequence of strong light bending by the extreme gravitational fields very close to the central black hole and is thus a prediction of general relativity. This may indicate that a complicated temporal behaviour of the iron line profiles seen in future data may not necessary imply a complicated model but could be explained for example in the framework of the orbiting flare model.

4 ACKNOWLEDGMENTS

MR acknowledges support from an External Research Studentship of Trinity College, Cambridge; an ORS award; and the Stefan Batory Foundation. MR thanks Andrew Fabian and Andrew Young for discussions.

REFERENCES

Abramowicz M.A., Lanza A., Spiegel E.A., Szuszkiewicz E., 1992, Nature, 356, 41
Bao G., 1992, A&A, 257, 594
Bardeen J.M., Peterson J.A., 1975, ApJL, 195, L65
Bardeen J.M., Press W.H., Teukolsky S.A., 1972, ApJ, 178, 347
Bromley B.C., Chen K., Miller W.A., 1997, ApJ, 475, 57
Campana S., Stella L., 1993, MNRAS, 264, 395
Campana S., Stella L., 1995, MNRAS, 272, 585
Chagelishvili G.D., Lominadze J.G., Rogava A.D., 1989, ApJ, 347, 1100
Cunningham C.T., 1975, ApJ, 202, 788
Cunningham C.T., Bardeen J.M., 1973, ApJ, 183, 237
Dabrowski Y., Fabian A.C., Iwasawa K., Lasenby A.N., Reynolds C.S, 1997, MNRAS, 288, L11
Fabian A.C., Rees M.J., Stella L., White N.E., 1989, MNRAS, 238, 729
Frank J., King A.R., Raine D.J., 1995, Accretion Power in Astrophysics 2nd edition
Galeev A.A., Rosner R., Vaiana G.S., 1979, ApJ, 229,318
George I.M., Fabian A.C., 1991, MNRAS, 249, 352
Ghosh P., Abramowicz A., 1997, MNRAS, 292, 887
Iwasawa K., Fabian A.C., Reynolds C.S., Nandra K. Otani C., Inoue H., Hayashida K., Brandt W.N., Dotani T., Kunieda H., Matsuoka M., Tanaka Y.. 1996, MNRAS, 282, 1038
Karas V., Vokrouhlický D., Polnarev A.G., 1992, MNRAS, 259, 569
Laor A., 1991, ApJ, 376, 90
Lightman A.P., White T.R., 1988, ApJ, 335, 57
Martocchia A., Matt G., 1996, MNRAS, L53, 282
Matt G., Perola G.C., 1992, MNRAS, 259, 433
Matt G., Perola G.C., Piro L., 1991, A&A, 247, 25
McHardy I.M., 1989, Proc. 23rd ESLAB Symposium on X-ray Astronomy, ESA SP-296, 1989
Mushotzky R.F., Fabian A.C., Iwasawa K., Kunieda H., Matsuoka M., Nandra K., Tanaka Y., 1995, MNRAS, 272, L9
Nandra K., George I.M., Mushotzky R.F., Turner T.J., Yaqoob T., 1997, ApJ, 477, 602
Livio M., Ogilvie G.I., Pringle J.E., 1999, ApJ, 512, 100
Pounds K.A., Nandra K., Steward G.C., George I.M., Fabian A.C., 1990, Nature, 344, 132
Rees M.J., Begelman M.C., Blandford R.D., Phinney E.S., 1982, Nature, 295, 17
Reynolds C.S., Begelman M.C., 1997, ApJ, 488, 109
Reynolds C.S., Young A.J., Begelman M.C., Fabian A.C, 1999, ApJ, 514, 164
Różańska A., Czerny B., Życki P.T., Pojmański G., 1998, MNRAS, submitted
Stella L., 1990, Nature, 344, 747
Tanaka Y., Nandra K., Fabian A.C., Inoue H., Otani C., Dotani T., Hayashida K., Iwasawa K., Kii T., Kunieda H., Makino F., Matsuoka M., 1995, Nature, 375, 659
Vries de M., Kuijpers J., 1992, A&A, 266, 77
Wilson A.S., Colbert E.J.M., 1995, ApJ, 438, 62
Young A.J., Ross R.R, Fabian A.C., 1998, MNRAS, 300, 11
Zakharov A.F., 1994, MNRAS, 269, 283

APPENDIX A1: THE KERR METRIC

Space-time in the vicinity of a rotating black hole is described by the Kerr metric. In Boyer-Lindquist coordinates this metric reads:

$$\begin{aligned} ds^2 &= -\left(1-\frac{2r}{\Sigma}\right)dt^2 - \frac{4ar}{\Sigma}\sin^2\theta dt d\phi + \frac{\Sigma}{\Delta}dr^2 + \Sigma d\theta^2 \\ &\quad + \frac{A}{\Sigma}\sin^2\theta d\phi^2, \end{aligned}$$

where

$$\Sigma = r^2 + a^2\cos^2\theta$$

$$\Delta = r^2 + a^2 - 2r$$

$$A = (r^2+a^2)^2 - a^2\Delta\sin^2\theta$$

APPENDIX A2: THE CONSTANTS OF MOTION FOR THE OFF-AXIS SOURCE ON A SPATIALLY CIRCULAR ORBIT

The photon trajectory may be specified by two constants of motion (the component of angular momentum parallel to the symmetry axis l and the Carter constant Q) which can be expressed in terms of the direction cosines $e_{\hat{i}}$ of the photon momentum $\mathbf{k}$ and the comoving tetrad $\lambda_{\hat{i}}$.

$$e_{\hat{i}} = \frac{\mathbf{k}\cdot\lambda_{\hat{i}}}{(\mathbf{k}\cdot\mathbf{h}\cdot\mathbf{k})^{1/2}} \qquad\qquad \hat{i} = r,\theta$$

where $\mathbf{g}$ is the Kerr metric tensor and $\mathbf{h}$ is the transverse projecting operator defined by $\mathbf{h} = \mathbf{g} + \mathbf{u}\cdot\mathbf{u}$ and $\mathbf{u}$ denotes the four velocity of the source given by:

$$\mathbf{u} = C(\partial_t + \Omega\partial_\phi) \qquad\qquad \mathbf{u}\cdot\mathbf{u} = -1$$

where

$$C = \left[1 - \frac{2r}{\Sigma}(1 - a\Omega\sin^2\theta)^2 - (r^2+a^2)^2\Omega^2\sin^2\theta\right]^{-1/2}$$

and Ω is the angular velocity of the flare *defined* by:

$$\Omega \equiv \frac{1}{a + (r\sin\theta)^{3/2}}$$

Note that such a definition does not violate (for the parameters considered in Section 3) the obvious condition that the source must follow a timelike worldline:

$$(\mathbf{u}\cdot\mathbf{u} = -1) \Rightarrow [g_{tt} + 2\Omega g_{\phi t} + \Omega^2 g_{\phi\phi}] < 0$$

The necessary components of the comoving tetrad and photon momentum are:

$$\lambda_{\hat{r}} = \left(\frac{\Delta}{\Sigma}\right)^{1/2}\partial_r$$

$$\lambda_{\hat{\theta}} = \Sigma^{-1/2}\partial_\theta$$

and

$$k^t = \frac{A}{\Delta\Sigma}(1 - l\omega)$$

$$k^r = \pm\frac{1}{\Sigma}\left[(2r-al)^2 + \Delta(r(r+2) - L)\right]^{1/2}$$

$$k^\theta = \pm\frac{1}{\Sigma}\left(L - \frac{l^2}{\sin^2\theta} + a^2\cos^2\theta\right)^{1/2}$$

$$k^\phi = \frac{A}{\Delta\Sigma}\left[\left(\frac{\Sigma - 2r}{A}\right)\frac{l}{\sin^2\theta} + \omega\right]^{1/2},$$

where $\omega = 2ar/A$ is the angular velocity of the frame dragging and $L = Q + l^2$. The directional cosines can be expressed as functions of polar Ψ and azimuthal Φ angles in the rest frame of the source in the usual way:

$$e_{\hat{r}} = \cos\Psi$$

$$e_{\hat{\theta}} = \sin\Psi\cos\Phi$$

Here we chose the local z axis to point in the ∂_r direction and the local x axis in ∂_θ direction. We can now combine the above equations to obtain the desired set of two equations for the two constants of motion l and Q:

$$\Sigma(e_{\hat{r}}^2 + e_{\hat{\theta}}^2)\mathbf{k}\cdot\mathbf{h}\cdot\mathbf{k} + \frac{l^2}{\sin^2\theta} = \frac{(2r-al)^2}{\Delta} + r(r+2) \qquad \text{(A1)}$$

$$\frac{e_{\hat{r}}^2}{e_{\hat{\theta}}^2}(a^2\cos^2\theta - \frac{l^2}{\sin^2\theta} + L) + L = \frac{(2r-al)^2}{\Delta} + r(r+2) \qquad \text{(A2)}$$

All components containing L in Eq. B1 cancel out miraculously and we obtain relatively simple quadratic equation for l which has the solution:

$$l = -\frac{Y}{2X} + \frac{1}{2}\mathrm{sgn}(\pi - \Phi)\left[\left(\frac{Y}{X}\right)^2 - 4\left(\frac{Z}{X}\right)\right]^{1/2}$$

with

$$X = \left(\frac{A}{\Delta\Sigma}\right)^2\left[qp(\omega)\left(\frac{A}{\Sigma}\sin^2\theta\right)^{-1} + C^2\left[(\Omega-\omega)q + p(\Omega)\omega\right]^2\right]$$
$$-\frac{1}{\Sigma}\left(\frac{a^2}{\Delta} - \frac{1}{\sin^2\theta}\right)f(\Psi,\Phi)$$

$$Y = 2\left(\frac{A}{\Delta\Sigma}\right)^2\left[\omega p(\omega) + C^2\left(\frac{A}{\Sigma}\omega(\Omega-\omega)^2 q\sin^2\theta - p^2(\Omega)\omega\right.\right.$$
$$\left.\left.-(\Omega-\omega)p(\Omega)p(-\omega)\right)\right] + \frac{4ar}{\Delta\Sigma}f(\Psi,\Phi)$$

$$Z = -\frac{1}{\Sigma}\left(\frac{4r^2}{\Delta} + r(r+2) + a^2\cos^2\theta\right)f(\Psi,\Phi)$$
$$+\left(\frac{A}{\Delta\Sigma}\right)^2 p(\omega)(C^2 p(\omega) - 1),$$

where

$$p(x) = 1 - \frac{2r}{\Sigma} + \frac{A}{\Sigma}\omega x\sin^2\theta, \qquad f(\Psi,\Phi) = \frac{\sin^2\Psi\sin^2\Phi}{1 - \sin^2\Psi\sin^2\Phi}$$

and $q = 1 - (2r/\Sigma)$. The second constant of motion $Q = L - l^2$ can be easily calculated from Eq. B2.

APPENDIX A3: ILLUMINATION OF THE DISC AND LIGHT CURVE FORMULAE

The observed flux consists of two elements: the direct flux from the flare and the reflected flux from the accretion disc. Let us first consider the observed flux $F(E_d)$ as seen by the disc element moving with the accretion flow.

$$F(E_d) = \frac{E_d dN_{E_d}}{dS}, \qquad \text{(A3)}$$

where E_d is the photon energy in the matter rest frame and dN_{E_d} is the number of photons per erg per second which illuminate an element of surface dS on the accretion disc. Because the number of photons has to be conserved and $dt_d dE_d = dt_e dE_e$ we have $dN_{E_d} = dN_{E_e}$, where the subscript e and d denote the rest frame of the flare and the disc frame respectively. Thus Eq. C1 takes the form:

$$F(E_d) = \frac{g_{sd}L_{E_e}}{dS}\frac{d\Omega_e}{4\pi},$$

where $d\Omega_e = 4\pi(dN_{E_e}/N_{tot})$ is the solid angle in the rest frame of the emitter which corresponds to the surface element dS on the disc, dN_{Ee} is the number of photons emitted into this solid angle, g_{sd} is the redshift factor and L_{E_e} is the luminosity of the source per unit energy. Note that in special relativity the transformation law for the solid angle is $d\Omega_e = g_{sd}^2 d\Omega_{obs}$. This means that in this regime we can recover the usual result $F_{tot} \propto g_{sd}^4$ by integrating the formula for the flux received by the disc element. Since

the surface density of photons is locally constant we have $dS = (dN_{E_e}/d\tilde{N}_{E_e})d\tilde{S}$, where $d\tilde{S} = \gamma(A/\Delta)^{1/2}d\phi dr$ is the surface area of the fixed grid element on the disc and γ is the Lorentz factor of the relative motion of the disc element and the locally non-rotating observer. For $r \leq r_{ms}$, where r_{ms} is the radius of marginal stability, this factor is given by:

$$\gamma = (1 - V^{(\phi)2})^{-1/2},$$

where

$$V^{(\phi)} = [A/(\Sigma\Delta^{1/2})](\Omega_e - \omega), \qquad \Omega_e = 1/(r^{3/2} + a),$$

whereas for $r_h < r < r_{ms}$, where r_h is the radius of the event horizon:

$$\gamma = (1 - \tilde{V}^{(r)2} - \tilde{V}^{(\phi)2})^{-1/2},$$

where

$$\tilde{V}^{(r)} = \frac{A^{1/2}}{\Delta}\frac{u^r}{u^t}$$

$$\tilde{V}^{(\phi)} = \frac{A}{\Delta^{1/2}\Sigma}\left(\frac{u^\phi}{u^t} - \omega\right).$$

The variables u^t, u^r and u^ϕ are the components of the 4-velocity below the innermost stable orbit (see e.g. Cunningham 1975) and V^ϕ, $\tilde{V}^r$ and $\tilde{V}^\phi$ are the components of 3-velocity relative to the locally non-rotating frame which can be calculated from $\tilde{V}^{(j)} = (u^\mu e^{(j)}_\mu)/(u^\nu e^{(t)}_\nu)$, where $j = r, \phi$ and $e^{(\nu)}_\mu$ are the components of the basis of one-forms corresponding to the set of basis vectors of the locally non-rotating observer (see Bardeen, Press, Teukolsky, 1972). Thus for the luminosity in the form of the power law $L_{E_e} \propto E_e^{-\alpha}$ we get:

$$F(E_d) \propto S_{E_d} = g_{sd}^{1+\alpha}E_d^{-\alpha}\frac{f_{sd}}{\gamma d\phi dr}\left(\frac{\Delta}{A}\right)^{1/2},$$

where $f_{sd} = d\tilde{N}_{E_d}/N_{tot}$ is the fraction of N_{tot} which corresponds to the grid element defined by $d\phi$ and dr. Assuming isotropic reflection, the final expressions for the reflected component of the flux read:

$$F_R(t) = \sum_n F_R^{(n)}(t),$$

where $F_R^{(n)}(t)$ is the contribution to the flux from the flare at n-th position given by:

$$F_R^{(n)}(\tilde{t}) = \frac{1}{\Delta\tilde{t}}\sum_{\tilde{t}\to\tilde{t}+\Delta\tilde{t}} C(E_{o1}, E_{o2}, \alpha)\int\int_{E_{o1}}^{E_{o2}} g_{do}^3 I_R(E_o/g_{do})dE_o\frac{dxdy}{r_o^2},$$

where $\tilde{t}$ is the sum of the time $\tilde{t}_{sd}$ it takes for the photon emitted at the source to reach a given element on the disc and the photon arrival time $\tilde{t}_{do}$ from that particular point on the disc to the observer. g_{do} is the redshift factor for the disc-to-observer case, C is the proportionality coefficient which depends on the energy index and the observed spectral band, $\Delta\tilde{t}$ is the width of the time bin and

$$I_R(E_o/g_{do}) = \frac{1}{\pi}a_R(\xi, E_d)F(E_d),$$

where $a_R(\xi, E)$ is the albedo of the reflecting material. We used the transformation law for the intensity $I_{E_o} = g_{sd}^3 I_{E_e}$ in the expression for $F_R^{(n)}$ above. Note that in the formula for $F_R^{(n)}$ we include contributions from all photon isodelay regions on the disc. We then interpolate $F_R^{(n)}$ at a given time t for all flare positions and sum these contributions to get the reflected flux $F_R(t)$. We use a very similar method to calculate the iron line spectra (appropriate formulae are given in the main text).

Analogously, we obtain the formula for the direct component of the flux in the following form:

$$F_D = C(E_{o1}, E_{o2}, \alpha)g_{so}^{1+\alpha}\frac{f_{so}}{\Delta x\Delta y}\int_{E_{o1}}^{E_{o2}} E_o^{-\alpha}dE_o,$$

where f_{so} is the fraction of the total number of emitted photons intersecting the observer's image plane which has the surface area $\Delta x\Delta y$. Note that the formulae for F_R and F_D have the same proportionality coefficient which enables us to compare the relative flux contributions.